

# Pseudospectral time-domain methods for modeling optical wave propagation in second-order nonlinear materials

Tae-Woo Lee and Susan C. Hagness

*Department of Electrical and Computer Engineering, University of Wisconsin, Madison, 1415 Engineering Drive, Madison, Wisconsin 53706*

Received March 6, 2003; revised manuscript received September 2, 2003; accepted September 16, 2003

Frequency conversion in second-order nonlinear materials is sensitive to the phase velocities of interacting optical waves. Accurate modeling of such problems with the finite-difference time-domain method requires extremely fine grid resolutions to minimize numerical dispersion errors. We propose an alternative approach based on a pseudospectral time-domain (PSTD) method for solving the nonlinear Maxwell's equations. Low-dispersion PSTD schemes with second- and fourth-order time stepping are developed and investigated. Benchmark simulations of second-harmonic generation (SHG) demonstrate that the PSTD schemes offer significant improvements in computational efficiency and accuracy. We demonstrate use of these schemes by modeling SHG in a nonlinear grating illuminated at an oblique angle, where phase matching is achieved in two dimensions. © 2004 Optical Society of America

OCIS codes: 190.0190, 190.2620, 000.4430

## 1. INTRODUCTION

Frequency conversion processes in second-order [ $\chi^{(2)}$ ] nonlinear materials such as  $\text{LiNbO}_3$  have been explored for a variety of optical communications, signal processing, data-storage, and sensing applications that rely on components such as wavelength routers, add-drop multiplexers, tunable coherent light sources, and all-optical switches.<sup>1-4</sup> Many of these nonlinear processes have been demonstrated in waveguiding structures designed with one-dimensional (1-D) quasi-phase-matching (QPM) techniques<sup>5</sup> to enhance the frequency conversion efficiency. Coupled-mode theory and beam propagation methods<sup>6-10</sup> have played important roles in the analysis and design of such structures. However, first-principles modeling tools based on the full-wave vector Maxwell's equations are needed for the analysis and design of more complicated nonlinear optical structures, such as two-dimensional (2-D) nonlinear photonic crystals.

One such modeling tool is the finite-difference time-domain (FDTD) method.<sup>11</sup> This technique, derived from finite-difference approximations in space and time, is based on volumetric sampling of the unknown electric and magnetic fields within and surrounding the structure of interest over a period time. The sampling in space is at a subwavelength resolution set by the user to properly sample the highest spatial frequencies thought to be important in the physics of the problem. The sampling in time is set by the Courant stability condition, which requires a bounding of the time step relative to the space increments. These requirements on the space and time increments have allowed the successful application of FDTD methods to a wide variety of linear electromagnetic wave modeling problems of moderate electrical size and quality factor. Examples include photonic bandgap structures,<sup>12-15</sup> microcavity ring and disk resonators,<sup>16,17</sup>

near-field scanning optical microscopy probes,<sup>18</sup> vertical-cavity surface-emitting lasers,<sup>19,20</sup> and diffractive optical elements.<sup>21</sup>

The FDTD method has been refined and extended over the past decade to treat a wide range of problems involving the interaction of electromagnetic waves with nonlinear materials.<sup>22-26</sup> It is ideally suited for the modeling of short-pulse phenomena in nonlinear media. As a time-domain technique, FDTD can also be used to calculate the complete nonlinear response of an electromagnetic system, including all harmonics generated by all frequency conversion processes as well as short-pulse phenomena in a nonlinear media. However, the numerical dispersion characteristics associated with FDTD can be problematic. Because interacting optical waves with different phase velocities will fall out of step as they propagate through a nonlinear material, a coarsely resolved FDTD simulation of a homogeneous frequency-independent second-order nonlinear material will erroneously predict a finite coherence length. A computationally inefficient solution to this problem is to use an extremely fine grid resolution to reduce the effects of numerical dispersion. For example, Bourgeade and Freysz reported that at least 80 points per wavelength at the second harmonic were required to achieve reasonably accurate results in their modeling of second-harmonic generation.<sup>25</sup>

In this paper we present an alternative solution to the problem of modeling phase-sensitive nonlinear optical phenomena—a solution in which we retain the advantages of the standard FDTD algorithm while simultaneously improving the computational efficiency. The proposed solution is based on the pseudospectral time-domain (PSTD) method<sup>27</sup> of solving the full-wave Maxwell's equations. Unlike the standard FDTD technique in which we use second-order-accurate finite-

difference approximations for the spatial derivatives, with PSTD we use the differentiation theorem for Fourier transforms to calculate the spatial derivatives. This spatial-differencing process converges with infinite order of accuracy for grid-sampling densities of two or more points per wavelength. Hence, the Yee-type leapfrog time stepping is the only source of numerical dispersion errors. We adapted the PSTD method in this paper for modeling optical wave propagation in  $\chi^{(2)}$  materials.

In Section 2 we review the standard second-order-accurate-in-time PSTD algorithm (denoted as PSTD-2) for linear media and propose a modified PSTD scheme with fourth-order time stepping (denoted as PSTD-4). We also compare the numerical dispersion relations and computational requirements of both schemes. In Section 3 we develop extensions of the PSTD algorithms for second-order nonlinear media. We evaluate the performance of the FDTD, PSTD-2, and PSTD-4 methods in Sections 4 and 5 using benchmark numerical simulations of nonlinear frequency conversion processes in a 1-D idealized (phase-matched) bulk nonlinear medium and a 2-D nonlinear waveguide with a QPM grating. In Section 6 we demonstrate use of the PSTD-4 scheme by modeling angle-dependent second-harmonic generation in a tilted QPM grating. In Section 7 we provide concluding remarks.

## 2. PSEUDOSPECTRAL TIME-DOMAIN METHOD

In contrast to the standard FDTD method where the spatial derivatives in Maxwell's curl equations are approximated by second-order-accurate central differences on a staggered, uncollocated Cartesian space lattice, with the PSTD method we use discrete Fourier transforms to evaluate the spatial derivatives on an unstaggered, collocated grid.<sup>27,28</sup> For example, the  $x$  derivative of a general field component  $\psi$  that is known at all grid points  $i$  along the  $x$  direction can be computed as follows:

$$\left. \frac{\partial \psi}{\partial x} \right|_i \approx F_x^{-1}[-jk_x F_x(\psi)]|_i, \quad (1)$$

where  $k_x$  is the Fourier-transform variable representing the  $x$  component of the numerical wave vector and  $F_x$  and  $F_x^{-1}$  denote, respectively, the forward and the inverse discrete Fourier transforms along the  $x$  direction. A fast-Fourier-transform (FFT) algorithm is used to implement approximation (1). The potential limitation caused by the periodic boundary conditions inherent in the FFT is eliminated by use of perfectly matched layer (PML) absorbing boundary conditions.<sup>29</sup> According to the Nyquist sampling theorem, the representation of approximation (1) is exact for grid-sampling densities of two or more per wavelength. Hence phase velocity errors in the PSTD method arise only from the Yee-type leapfrog time stepping.

We note that there is a potential difficulty with PSTD in the implementation of a spatially compact wave source condition. A source condition that is commonly used in time-domain simulations is one that specifies the field at a single grid point with a temporal driving function. This type of source, which represents a spatially dis-

cretized delta function, causes difficulties for the FFTs. However, we have shown that a spatially compact wave source condition spanning only two grid cells in each dimension completely eliminates the problem of Gibbs phenomena.<sup>30</sup>

### A. Pseudospectral Time-Domain Scheme with Second-Order-Accurate Time Stepping

Consider an electromagnetic wave propagating in a linear, lossless, nondispersive, and isotropic medium with no electric or magnetic current sources. The time differencing for PSTD as reported in Ref. 27 is based on standard second-order-accurate Yee leapfrogging as follows:

$$\mathbf{H}|_{i,j,k}^{n+1/2} = \mathbf{H}|_{i,j,k}^{n-1/2} - \frac{\Delta t}{\mu} (\nabla \times \mathbf{E})|_{i,j,k}^n, \quad (2)$$

$$\mathbf{E}|_{i,j,k}^{n+1} = \mathbf{E}|_{i,j,k}^n + \frac{\Delta t}{\epsilon} (\nabla \times \mathbf{H})|_{i,j,k}^{n+1/2}, \quad (3)$$

where subscripts  $i, j$ , and  $k$  are the Cartesian coordinate indices of the spatial sampling point ( $i\Delta x, j\Delta y, k\Delta z$ ) in the three-dimensional (3-D) lattice and  $n$  is the index of the temporal sampling point ( $n\Delta t$ ). Use of approximation (1) to evaluate the curl operators in Eqs. (2) and (3) yields time-stepping relations of the following form:

$$\begin{aligned} H_u|_{i,j,k}^{n+1/2} = & H_u|_{i,j,k}^{n-1/2} - \frac{\Delta t}{\mu_{i,j,k}} \{F_v^{-1}[-jk_v F_v(E_w)]|_{i,j,k}^n \\ & - F_w^{-1}[-jk_w F_w(E_v)]|_{i,j,k}^n\}, \end{aligned} \quad (4)$$

$$\begin{aligned} E_u|_{i,j,k}^{n+1} = & E_u|_{i,j,k}^n + \frac{\Delta t}{\epsilon_{i,j,k}} \{F_v^{-1}[-jk_v F_v(H_w)]|_{i,j,k}^{n+1/2} \\ & - F_w^{-1}[-jk_w F_w(H_v)]|_{i,j,k}^{n+1/2}\}, \end{aligned} \quad (5)$$

where  $(u, v, w) = (x, y, z), (y, z, x)$ , and  $(z, x, y)$ . To emphasize the second-order-accurate nature of the time stepping, we denote this method as PSTD-2.

### B. Pseudospectral Time-Domain Scheme with Fourth-Order-Accurate Time Stepping

Taylor-series expansions of a general field component  $\psi$  about time step  $n$  yield the following fourth-order-accurate centered finite-difference approximation for the time derivative of  $\psi$ <sup>31</sup>:

$$\left. \frac{\partial \psi}{\partial t} \right|^n = \frac{\psi|^{n+1/2} - \psi|^{n-1/2}}{\Delta t} - \frac{\Delta t^2}{24} \frac{\partial^3 \psi}{\partial t^3} \Big|_n + O(\Delta t^4). \quad (6)$$

Applying Eq. (6) to the time derivatives in Maxwell's curl equations yields

$$\mathbf{H}|_{i,j,k}^{n+1/2} = \mathbf{H}|_{i,j,k}^{n-1/2} - \frac{\Delta t}{\mu} (\nabla \times \mathbf{E})|_{i,j,k}^n + \frac{\Delta t^3}{24} \frac{\partial^3 \mathbf{H}}{\partial t^3} \Big|_{i,j,k}^n, \quad (7)$$

$$\begin{aligned} \mathbf{E}|_{i,j,k}^{n+1} &= \mathbf{E}|_{i,j,k}^n + \frac{\Delta t}{\epsilon} (\nabla \times \mathbf{H})|_{i,j,k}^{n+1/2} \\ &+ \frac{\Delta t^3}{24} \frac{\partial^3 \mathbf{E}}{\partial t^3} \Big|_{i,j,k}^{n+1/2}. \end{aligned} \quad (8)$$

Rather than calculate  $\partial^3 \mathbf{H}/\partial t^3$  and  $\partial^3 \mathbf{E}/\partial t^3$  directly, we convert the time derivatives in Eqs. (7) and (8) to spatial derivatives using Maxwell's curl equations as follows:

$$\frac{\partial^3 \mathbf{H}}{\partial t^3} \Big|_{i,j,k}^n = -\frac{1}{\mu} \nabla \times \left[ \frac{1}{\epsilon} \nabla \times \left( -\frac{1}{\mu} \nabla \times \mathbf{E} \right) \right] \Big|_{i,j,k}^n, \quad (9)$$

$$\frac{\partial^3 \mathbf{E}}{\partial t^3} \Big|_{i,j,k}^{n+1/2} = \frac{1}{\epsilon} \nabla \times \left[ -\frac{1}{\mu} \nabla \times \left( \frac{1}{\epsilon} \nabla \times \mathbf{H} \right) \right] \Big|_{i,j,k}^{n+1/2}. \quad (10)$$

Substituting Eqs. (9) and (10) into Eqs. (7) and (8) and computing all spatial derivatives using the approach of approximation (1), we obtain a complete PSTD algorithm with fourth-order time stepping, which we denote as PSTD-4.

We note that the numerical evaluation of the nested curl operations in Eqs. (9) and (10) requires an extremely large number of FFT subroutine calls. The computational complexity of implementing Eqs. (7) and (8) using Eqs. (9) and (10) can be greatly reduced when we make the assumption that the spatial variation of the material properties at each field sampling point  $(i, j, k)$  is small such that  $\nabla(\epsilon^{-1}) \approx 0$  and  $\nabla(\mu^{-1}) \approx 0$ . This assumption permits the simplification of the nested curl operators. In this case, the set of time-stepping relations becomes

$$\begin{aligned} \mathbf{H}|_{i,j,k}^{n+1/2} &= \mathbf{H}|_{i,j,k}^{n-1/2} - \frac{\Delta t}{\mu} (\nabla \times \mathbf{E})|_{i,j,k}^n \\ &+ \frac{\Delta t^3}{24} \left( \frac{v^2}{\mu} \nabla \times \nabla \times \nabla \times \mathbf{E} \right) \Big|_{i,j,k}^n, \end{aligned} \quad (11)$$

$$\begin{aligned} \mathbf{E}|_{i,j,k}^{n+1} &= \mathbf{E}|_{i,j,k}^n + \frac{\Delta t}{\epsilon} (\nabla \times \mathbf{H})|_{i,j,k}^{n+1/2} \\ &- \frac{\Delta t^3}{24} \left( \frac{v^2}{\epsilon} \nabla \times \nabla \times \nabla \times \mathbf{H} \right) \Big|_{i,j,k}^{n+1/2}, \end{aligned} \quad (12)$$

where  $v = 1/\sqrt{\mu\epsilon}$ . We show that this simplified PSTD-4 algorithm offers a significant improvement in accuracy over PSTD-2 even for models with material inhomogeneities.

### C. Comparison of PSTD-2 and PSTD-4 Computational Requirements

In the 1-D case with  $E_z$  polarization and  $x$ -directed propagation, Eqs. (11) and (12) reduce to the following PSTD-4 updating equations:

$$\begin{aligned} H_y|_i^{n+1/2} &= H_y|_i^{n-1/2} + \frac{\Delta t}{\mu_i} \left\{ F_x^{-1}[-jk_x F_x(E_z)]|_i^n \right. \\ &+ \left. \frac{v_{i,j}^2 \Delta t^2}{24} F_x^{-1}[jk_x^3 F_x(E_z)]|_i^n \right\}, \end{aligned} \quad (13)$$

$$\begin{aligned} E_z|_i^{n+1} &= E_z|_i^n + \frac{\Delta t}{\epsilon_i} \left\{ F_x^{-1}[-jk_x F_x(H_y)]|_i^{n+1/2} \right. \\ &+ \left. \frac{v_{i,j}^2 \Delta t^2}{24} F_x^{-1}[jk_x^3 F_x(H_y)]|_i^{n+1/2} \right\}. \end{aligned} \quad (14)$$

Note that without the last term in Eqs. (13) and (14), they reduce to the PSTD-2 algorithm for one dimension. The presence of these terms in PSTD-4 adds more FFT subroutine calls per time step compared with PSTD-2. Specifically, to update either  $H_y$  or  $E_z$ , one forward and two inverse FFTs are required in PSTD-4 whereas with PSTD-2 we use one forward and one inverse FFT. Hence, in one dimension, PSTD-4 requires a total of six FFT subroutine calls per grid cell per time step whereas PSTD-2 requires a total of only four.

In the 2-D case with  $\text{TM}_z$  polarization, the PSTD-4 updating equations are given by

$$\begin{aligned} H_x|_{i,j}^{n+1/2} &= H_x|_{i,j}^{n-1/2} - \frac{\Delta t}{\mu_{i,j}} \left\{ F_y^{-1}[-jk_y F_y(E_z)]|_{i,j}^n \right. \\ &+ \frac{v_{i,j}^2 \Delta t^2}{24} [F_x^{-1}(-k_x^2 F_x \{F_y^{-1} \\ &\times [-jk_y F_y(E_z)]\})|_{i,j}^n \\ &+ \left. F_y^{-1}[jk_y^3 F_y(E_z)]|_{i,j}^n \right\}, \end{aligned} \quad (15)$$

$$\begin{aligned} H_y|_{i,j}^{n+1/2} &= H_y|_{i,j}^{n-1/2} + \frac{\Delta t}{\mu_{i,j}} \left\{ F_x^{-1}[-jk_x F_x(E_z)]|_{i,j}^n \right. \\ &+ \frac{v_{i,j}^2 \Delta t^2}{24} [F_y^{-1}(-k_y^2 F_y \{F_x^{-1} \\ &\times [-jk_x F_x(E_z)]\})|_{i,j}^n \\ &+ \left. F_x^{-1}[jk_x^3 F_x(E_z)]|_{i,j}^n \right\}, \end{aligned} \quad (16)$$

$$\begin{aligned} E_z|_{i,j}^{n+1} &= E_z|_{i,j}^n + \frac{\Delta t}{\epsilon_{i,j}} \left\{ F_x^{-1}[-jk_x F_x(H_y)]|_{i,j}^{n+1/2} \right. \\ &- F_y^{-1}[-jk_y F_y(H_x)]|_{i,j}^{n+1/2} \\ &+ \frac{v_{i,j}^2 \Delta t^2}{24} [2F_y^{-1}(-k_y^2 F_y \{F_x^{-1} \\ &\times [-jk_x F_x(H_y)]\})|_{i,j}^{n+1/2} \\ &+ F_x^{-1}[jk_x^3 F_x(H_y)]|_{i,j}^{n+1/2} \\ &- \left. F_y^{-1}[jk_y^3 F_y(H_x)]|_{i,j}^{n+1/2} \right\}, \end{aligned} \quad (17)$$

where Gauss's law in two dimensions ( $\partial H_x/\partial x = -\partial H_y/\partial y$ ) was used to reduce the number of terms in

Eq. (17). The 2-D TE<sub>z</sub> case can be obtained directly from Eqs. (15)–(17) by use of the duality of  $\mathbf{E}$  and  $\mathbf{H}$ . Once again, the PSTD-4 updating equations have additional terms beyond those that appear in the PSTD-2 equations. In counting the number of FFTs required by PSTD-4, we note that some of the FFTs appear more than once in each equation. For example, in Eq. (15),  $F_y(E_z)$  appears three times and  $F_y^{-1}[-jk_y F_y(E_z)]$  appears twice. Obviously, these duplicate FFTs have to be computed only once. Therefore PSTD-4 requires a total of two forward and three inverse FFT subroutine calls to update  $H_x$ . Overall, PSTD-4 requires a total of 18 FFT subroutine calls per grid cell per time step whereas PSTD-2 uses only eight.

In the 3-D case, two of the six updating equations are presented to illustrate the computational requirements:

$$\begin{aligned}
 H_x|_{i,j,k}^{n+1/2} &= H_x|_{i,j,k}^{n-1/2} - \frac{\Delta t}{\mu_{i,j,k}} \\
 &\times \left( E_z^{\partial y}|_{i,j,k}^n - E_y^{\partial z}|_{i,j,k}^n \right. \\
 &+ \frac{v_{i,j,k}^2 \Delta t^2}{24} \{ F_y^{-1}[jk_y^3 F_y(E_z)]|_{i,j,k}^n \\
 &- F_z^{-1}[jk_z^3 F_z(E_y)]|_{i,j,k}^n \\
 &+ F_x^{-1}[-k_x^2 F_x(E_z^{\partial y})]|_{i,j,k}^n \\
 &+ F_z^{-1}[-k_z^2 F_z(E_z^{\partial y})]|_{i,j,k}^n \\
 &- F_x^{-1}[-k_x^2 F_x(E_y^{\partial z})]|_{i,j,k}^n \\
 &\left. - F_y^{-1}[-k_y^2 F_y(E_y^{\partial z})]|_{i,j,k}^n \right\}, \quad (18)
 \end{aligned}$$

$$\begin{aligned}
 E_x|_{i,j,k}^{n+1} &= E_x|_{i,j,k}^n - \frac{\Delta t}{\epsilon_{i,j,k}} \\
 &\times \left( H_z^{\partial y}|_{i,j,k}^{n+1/2} - H_y^{\partial z}|_{i,j,k}^{n+1/2} \right. \\
 &+ \frac{v_{i,j,k}^2 \Delta t^2}{24} \{ F_y^{-1}[jk_y^3 F_y(H_z)]|_{i,j,k}^{n+1/2} \\
 &- F_z^{-1}[jk_z^3 F_z(H_y)]|_{i,j,k}^{n+1/2} \\
 &+ F_x^{-1}[-k_x^2 F_x(H_z^{\partial y})]|_{i,j,k}^{n+1/2} \\
 &+ F_z^{-1}[-k_z^2 F_z(H_z^{\partial y})]|_{i,j,k}^{n+1/2} \\
 &- F_x^{-1}[-k_x^2 F_x(H_y^{\partial z})]|_{i,j,k}^{n+1/2} \\
 &\left. - F_y^{-1}[-k_y^2 F_y(H_y^{\partial z})]|_{i,j,k}^{n+1/2} \right\}, \quad (19)
 \end{aligned}$$

where  $u_\eta^{\partial \zeta} \equiv F_\zeta^{-1}[-jk_\zeta F_\zeta(u_\eta)]$  for  $u \equiv \{E, H\}$  and  $(\eta, \zeta) \equiv \{x, y, z\}$ . Overall, PSTD-4 requires a total of 84 FFT subroutine calls per grid cell per time step to update all six field components in three dimensions whereas PSTD-2 uses only 24.

Table 1 summarizes the computational requirements of PSTD-2 and PSTD-4. Because most of the CPU time is spent on FFT routines with the PSTD methods, the data

**Table 1. Number of FFT Subroutine Calls Required per Grid Cell per Time Step**

Method	1-D	2-D	3-D
PSTD-2	4	8	24
PSTD-4	6	18	84

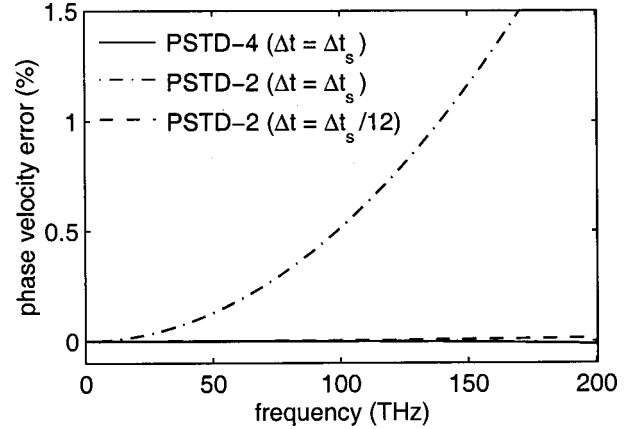


Fig. 1. Comparison of the free-space numerical phase velocity errors associated with the PSTD-2 and PSTD-4 schemes.

in Table 1 can be used to determine the computational overhead per time step of PSTD-4 relative to PSTD-2. For example, in one dimension, PSTD-4 requires 1.5 times more FFT routines per time step than PSTD-2. This computational overhead factor increases to 2.25 in two dimensions and 3.5 in three dimensions. These factors are used to discuss the efficiency of PSTD-4 compared with PSTD-2 in Subsection 2.D.

#### D. Comparison of the Numerical Accuracy of PSTD-2 and PSTD-4

Consider a sinusoidal numerical plane wave of angular frequency  $\omega$  propagating in an arbitrary direction within a 3-D free-space lattice. The following numerical dispersion relation<sup>27</sup> for PSTD-2 was derived for this case:

$$\tilde{k} = \frac{2}{c \Delta t} \sin\left(\frac{\omega \Delta t}{2}\right). \quad (20)$$

Here  $\tilde{k}$  represents the numerical wave number. Following a procedure similar to that presented in Ref. 27, we derive the following numerical dispersion relation for the PSTD-4 method:

$$\tilde{k} \left[ 1 - \left( \frac{c^2 \Delta t^2}{24} \right) \tilde{k}^2 \right] = \frac{2}{c \Delta t} \sin\left(\frac{\omega \Delta t}{2}\right). \quad (21)$$

We note that, without the  $\Delta t^2$  term on the left-hand side, Eq. (21) reduces to the numerical dispersion relation for PSTD-2.

To compare the numerical dispersion properties of PSTD-2 and PSTD-4, we compute the numerical phase velocity  $\bar{v} = \omega/\tilde{k}$  using Eqs. (20) and (21), assuming a 2-D

grid. The error in the numerical phase velocity is plotted in Fig. 1 over a frequency range from dc to 200 THz. The assumed grid resolution corresponds to four cells per wavelength at  $f_{\max} = 200$  THz for both PSTD-2 and PSTD-4. First, a time step corresponding to the 2-D stability limit<sup>27</sup> for a square grid lattice ( $\Delta x = \Delta y$ ) is assumed for both PSTD-2 and PSTD-4:

$$\Delta t_s = \frac{2\Delta x}{\pi c \sqrt{2}}. \quad (22)$$

For this maximum time step, the numerical phase velocity error associated with PSTD-4 (solid line in Fig. 1) is 0.013% at  $f_{\max}$ , which is two orders of magnitude smaller than the 2.16% error associated with PSTD-2 at  $f_{\max}$  (dashed-dotted curve in Fig. 1). Next, the assumed time step of PSTD-2 is decreased to the point at which a level of accuracy similar to PSTD-4 is achieved. The dashed line in Fig. 1 represents the numerical phase velocity error computed for PSTD-2 with a time step that is 12 times smaller than that assumed for the PSTD-4 case. With  $\Delta t = \Delta t_s/12$ , PSTD-2 exhibits an error of 0.014% at  $f_{\max}$ .

Because PSTD-4 offers higher accuracy than PSTD-2 for a fixed time step, the computational overhead factors of Subsection 2.C should be reconsidered. As shown in Table 1, PSTD-2 is more computationally efficient than PSTD-4 per time step. However, as shown in Fig. 1, PSTD-2 requires a much smaller time step to achieve the same level of accuracy offered by PSTD-4. Thus PSTD-4 offers improved computational efficiency over PSTD-2 as long as the computational overhead per time step of PSTD-4 relative to PSTD-2 is compensated by the reduction in the total number of time steps required by PSTD-4 relative to PSTD-2. The break-even point in the computational burden of PSTD-4 versus PSTD-2 occurs when the accuracy requirements of the problem forces PSTD-2 to have a time step that is 1.5, 2.25, and 3.5 times smaller than that used by PSTD-4 in one, two, and three dimensions, respectively. For example, in the 2-D case of Fig. 1 where PSTD-2 requires a time step that is approximately 12 times smaller than that used by PSTD-4 to achieve the same level of accuracy, PSTD-4 is approximately 5.33 (=12/2.25) times more computationally efficient than PSTD-2 in time marching the simulation to the same end point in physical time.

### 3. EXTENSION TO SECOND-ORDER NONLINEAR MEDIA

In this section we present an extension of the PSTD algorithm that permits the modeling of electromagnetic wave propagation in a medium exhibiting a large instantaneous second-order nonlinearity. We limit the discussion here to cases in which there is only one electric field component (such as the  $\text{TM}_z$  mode in a 2-D grid comprised of the  $x$ - $y$  plane).

In contrast to the linear case in which one time step in the two-stage PSTD numerical solution consists of our updating  $H$  from the previously computed  $E$  using Faraday's law and updating  $E$  from the previously computed  $H$  using Ampere's law, the PSTD scheme for the nonlinear case becomes a three-stage process to complete one time step.

In the first stage, we update  $H$  from  $E$  using Faraday's law. In the second stage, we update the electric flux density  $D$  from  $H$  using Ampere's law. Note that, for PSTD-2, Eq. (3) must be modified to account for the updating of  $D$  rather than  $E$ . Likewise, for PSTD-4, Eq. (8) and all subsequent equations derived from Eq. (8) must be modified. In the third and final stage, we update  $E$  from  $D$  using the following constitutive relation:

$$D = \epsilon_0 \epsilon_r E + \epsilon_0 \chi^{(2)} E^2, \quad (23)$$

where  $\chi^{(2)}$  is the second-order nonlinear susceptibility of the medium. We can apply an iterative method<sup>26</sup> proposed in the context of FDTD to Eq. (23) to solve for the latest value of  $E$  using the newly updated value of  $D$  and the old value of  $E$  as follows:

$$E = \frac{D}{\epsilon_0 [\epsilon_r + \chi^{(2)} E]}. \quad (24)$$

Note that Eq. (24) is also valid in a linear medium where  $\chi^{(2)} = 0$ . As an alternative to Eq. (24), the following equation can be used to achieve a noniterative, direct solution of Eq. (23):

$$E = \frac{-\epsilon_0 \epsilon_r + [(\epsilon_0 \epsilon_r)^2 + 4\epsilon_0 \chi^{(2)} D]^{1/2}}{2\epsilon_0 \chi^{(2)}}. \quad (25)$$

In Eq. (25), the solution with the positive sign in front of the square root was chosen because this solution reproduces the proper relationship between  $E$  and  $D$  in the limit as  $\chi^{(2)} \rightarrow 0$ . Note, however, that Eq. (25) must be replaced by the linear constitutive relation  $E = D/(\epsilon_0 \epsilon_r)$  in any region of the grid where  $\chi^{(2)} = 0$ .

We conclude this section with a clarification relevant to the nonlinear PSTD-4 algorithm. Because of the nonlinear constitutive relation, the higher-order time derivatives in Eq. (7) and the electric flux density version of Eq. (8) can no longer be converted to pure spatial derivatives. For example, in one dimension, the time-to-space conversion equations analogous to Eqs. (9) and (10) are given by

$$\frac{\partial^3 H_y}{\partial t^3} = \frac{v^2}{\mu} \frac{\partial^3 E_z}{\partial x^3} - \frac{\chi^{(2)}}{\mu \epsilon_r} \frac{\partial^3 (E_z^2)}{\partial x \partial t^2}, \quad (26)$$

$$\frac{\partial^3 D_z}{\partial t^3} = v^2 \frac{\partial^3 H_y}{\partial x^3} - \frac{\chi^{(2)}}{\mu \epsilon_r} \frac{\partial^3 (E_z^2)}{\partial x^2 \partial t}. \quad (27)$$

We can preserve the computational simplicity of the PSTD-4 algorithm by neglecting the mixed derivative terms involving  $E_z^2$ . As demonstrated in Section 4, this simplification has a negligible effect on the accuracy of PSTD-4 relative to the PSTD-2 because the dominant nonlinear effect is already captured by Eq. (23).

### 4. PERFORMANCE EVALUATION: ONE-DIMENSIONAL SIMULATIONS

In this section we present the results of numerical experiments designed to test the performance of the PSTD-2 and PSTD-4 algorithms for 1-D wave propagation in linear and nonlinear media. Simulations in one dimension offer an ideal testing environment because phase-

sensitive nonlinear frequency conversion processes can be studied in the absence of waveguide dispersion. In such an environment, the only source of phase mismatch for waves propagating in a frequency-independent nonlinear medium is numerical dispersion.

### A. Linear Validations

First, we present a comparison of PSTD-2 and PSTD-4 simulations of pulse propagation in free space using a 1-D grid terminated with periodic boundary conditions. The spatial grid cell size is chosen to be  $\Delta x = \lambda_{\min}/10$ , and the time step is set at the 1-D stability limit ( $\Delta t_s = 2\Delta x/\pi c$ ). A Blackman-Harris pulse with a maximum frequency of 800 THz is chosen as the source excitation. A compact transparent wave source condition comprised of two current sources located at adjacent grid points is used to launch the pulse. (We note that a source that specifies a temporal driving function at a single grid point causes difficulties for the FFTs inherent in the PSTD algorithm. However, a compact source condition spanning two spatial grid cells avoids such difficulties and eliminates the problem of errors due to Gibbs phenomena.<sup>30</sup>) Figure 2 shows the electric field distribution throughout the grid at time step 10,000. At this point in the simulation, the pulse has propagated a distance of approximately 240  $\mu\text{m}$ . In the PSTD-2 simulation, numerical phase velocity errors have accumulated over many time steps, causing severe pulse distortion. However, the PSTD-4 simulation shows no visible effects of numerical dispersion. This result vividly illustrates the additional accuracy provided by PSTD-4 compared with PSTD-2.

Second, we present a comparison of the numerical dispersion errors inherent in PSTD-2 and PSTD-4 simulations as a function of the size of the time step. We conduct simulations of wave propagation in a free-space grid to extract the propagation constant  $\beta$ . For this test, the spatial grid cell size is chosen to be  $\Delta x = \lambda/10$ . Figure 3(a) shows the percent error in  $\beta$  for the PSTD-2 simulation. When the time step is set at  $0.8\Delta t_s$ , the error is 1.667%. When the time step is decreased to  $0.4\Delta t_s$ , the error drops to 0.418%. Hence the numerical data show that when  $\Delta t$  is decreased by 2:1, the error is reduced by

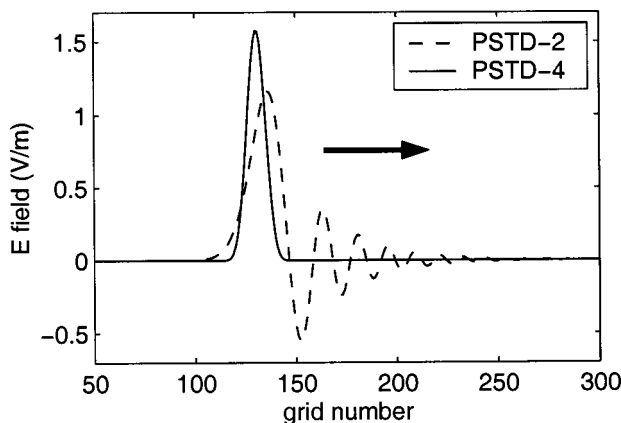
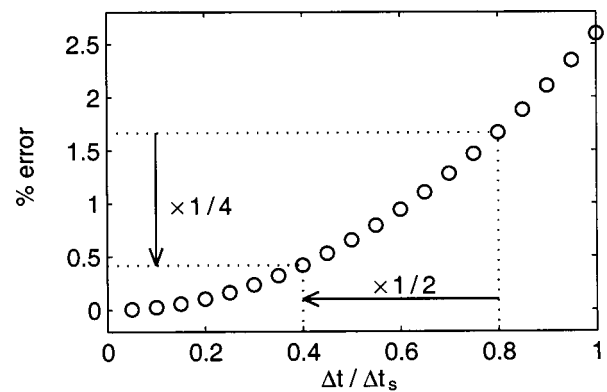
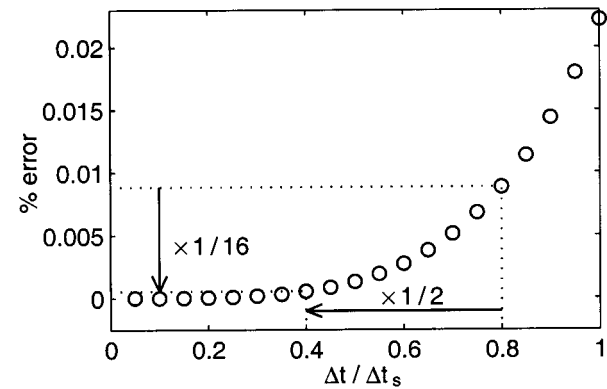


Fig. 2. Pulse propagation in a 1-D free-space grid with periodic boundary conditions. The electric field data are plotted after 10,000 time steps. The arrow indicates the direction of propagation.



(a)



(b)

Fig. 3. Percent error in the numerical propagation constant computed with 1-D PSTD simulations of wave propagation in free space. (a) In the PSTD-2 simulation, a decrease in the time step by 2:1 reduces the error by 4:1. (b) In the PSTD-4 simulation, a decrease in the time step by 2:1 reduces the error by 16:1.

approximately 4:1, indicative of the second-order-accurate time integration scheme we are using in the PSTD-2 algorithm. Figure 3(b) shows the percent error in  $\beta$  for the PSTD-4 simulation. Here, when the time step is decreased from 0.8 to  $0.4\Delta t_s$ , the error decreases from 0.00863% to 0.0005484%. We can see that reducing  $\Delta t$  by 2:1 cuts the error by approximately 16:1. This numerical data confirm our claim that the PSTD-4 algorithm is fourth-order accurate in time.

### B. Nonlinear Validations

Next we compare the performance of the PSTD-4, PSTD-2, and FDTD methods to model second-harmonic generation in a second-order nonlinear material. For this test case, we construct a homogeneous grid simulating a nonlinear dielectric ( $\epsilon_r = 4$  and  $\chi^{(2)} = 44 \text{ pm/V}$ ). The 1-D computational domain is terminated by uniaxial perfectly matched layer absorbing boundary conditions. We excited a ramped 200-THz sinusoidal signal at the far left side of the 1-D grid using the compact wave source condition of Ref. 30. The input power density of this fundamental wave is  $8 \times 10^{12} \text{ W/m}^2$ . The grid resolution is  $\Delta x = \lambda_d/20 = 37.5 \text{ nm}$ , where  $\lambda_d$  is the wavelength in the nonlinear dielectric corresponding to the fundamental (pumping) frequency component. The time step is set at a revised PSTD stability limit ( $\Delta t_s = 0.7 \times 2\Delta x/\pi c$ ),

which was reduced to avoid stability problems due to the nonlinearity.<sup>32</sup> The total physical simulation time is 2.1 ps.

Figure 4 shows the sinusoidal steady-state results from the PSTD-4 simulation after we calculated discrete Fourier transforms of the time-varying fields at every grid cell for five harmonic frequency components and converted to power density. The power density of the fundamental is steadily decreasing in the direction of propagation as some of its energy is converted to higher harmonics. This example illustrates the fact that a PSTD simulation (just like FDTD) inherently captures the effects of all frequency conversion processes.

In terms of the wavelength of the second harmonic, the grid-sampling density used in the PSTD-4 simulation is  $N = \lambda/\Delta x = 10$ . The PSTD-4 results for the second harmonic are already numerically converged for the largest time step used in this simulation, as shown in Fig. 5(a). Therefore the PSTD-4 results for the second harmonic are used as a benchmark to compare the PSTD-2 and FDTD methods. Figures 5(b) and 5(c) show the sinusoidal steady-state results for the second harmonic as computed by the PSTD-2 and FDTD methods, respectively.

In the PSTD-2 model, we use the same grid resolution used in the PSTD-4 simulation ( $N = 10$ ) and start with the same time step, repeating the simulation for smaller  $\Delta t$  until the power density distribution at a propagation distance of 300  $\mu\text{m}$  is numerically converged (i.e., less than 1.5% error with respect to the PSTD-4 result). The PSTD-2 time step required to achieve accuracy comparable to the PSTD-4 method is approximately ten times smaller than that used in the PSTD-4 simulation. In the FDTD model, we start with same grid resolution used in the PSTD-4 simulation and repeat the simulation for smaller  $\Delta x$  until convergence is reached (i.e., less than 1.5% error). The time step is maintained at 0.7 times the FDTD Courant limit. The FDTD grid-sampling density required to achieve comparable accuracy is approximately  $N = 140$ ; that is, the grid cell size is 14 times smaller than that used in the PSTD-4 simulation.

We compare the computational efficiency of these methods by calculating the total number of time steps required

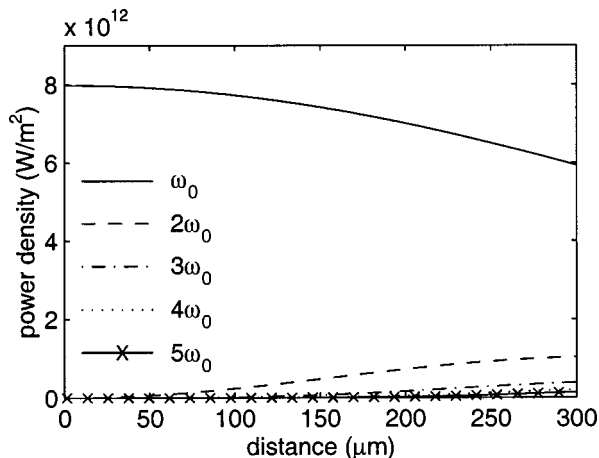


Fig. 4. Power density of the fundamental and higher harmonics as a function of propagation distance in a 1-D nondispersive second-order nonlinear material simulated with PSTD-4.

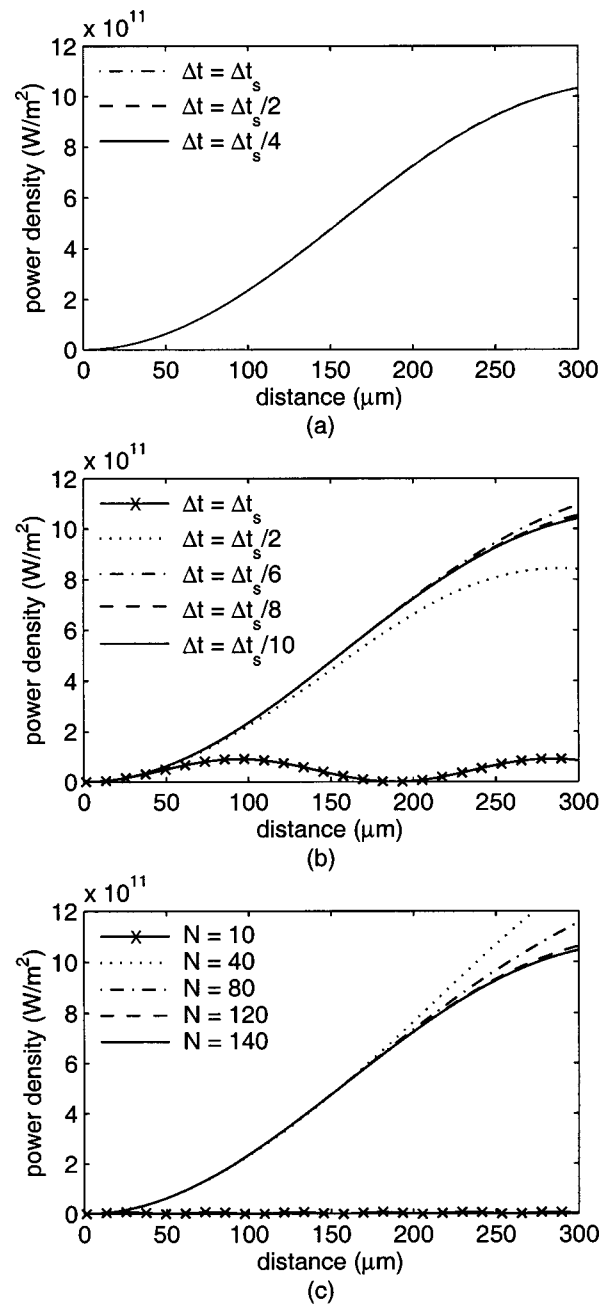


Fig. 5. Power density of the second harmonic as a function of propagation distance in a nondispersive second-order nonlinear material. (a) PSTD-4 results with various  $\Delta t$ , (b) PSTD-2 results with various  $\Delta t$ , (c) FDTD results with various grid-sampling densities.

to complete the simulation and the CPU time required per time step. The grid cell size and time step are chosen to suppress the error to less than 1.5% over the 300- $\mu\text{m}$  propagation distance. The total number of time steps required is 168,000 for FDTD and 188,400 for PSTD-2 whereas PSTD-4 requires only 18,840 time steps. The CPU times on a Sun Ultra 80 workstation are 16.5 ms/ $\Delta t$ , 4.9 ms/ $\Delta t$ , and 7.0 ms/ $\Delta t$  for FDTD, PSTD-2, and PSTD-4, respectively. Therefore, in this specific example, PSTD-4 is 7 times faster than PSTD-2 and 21 times faster than FDTD.

We note that errors due to numerical dispersion are cumulative; that is, they increase with distance of wave propagation. For example, if the propagation distance is only 100  $\mu\text{m}$ , then  $N = 40$  (a grid cell size four times smaller than that of PSTD-4) would yield acceptable results with FDTD and  $\Delta t = \Delta t_s/6$  (a time step six times smaller than that of PSTD-4) would yield acceptable results with PSTD-2. For the same reason, a simulation involving propagation over a distance farther than 300  $\mu\text{m}$  would require FDTD to have finer grid resolutions and PSTD-2 to have smaller time steps than PSTD-4. Hence the computational efficiency of the PSTD-4 method proposed here increases as the model size increases.

## 5. PERFORMANCE EVALUATION: TWO-DIMENSIONAL SIMULATIONS

In this section we present the results of numerical experiments designed to test the performance of our PSTD algorithms for 2-D wave propagation in the presence of material discontinuities and waveguide dispersion. Here, we model a 2-D symmetric dielectric slab waveguide assuming TE wave propagation. In Subsection 5.A we present validation studies for the case of a linear waveguide. In Subsection 5.B we present validation studies for the case in which the core guiding layer is comprised of a nonlinear material.

The idealized cross-sectional profile of the dielectric slab waveguide is illustrated by the dotted line in Fig. 6. This relatively large and abrupt transition of dielectric properties between the core and the cladding regions causes sharp lateral variations in some of the field components of the various waveguide modes at the interface between the core and the cladding. One such example is the magnetic field associated with the fundamental mode. In such cases, FFT-related errors arise because of the high spatial frequencies in the lateral direction across the waveguide. We can avoid these errors by choosing the lateral grid cell size to be small enough to adequately sample the sharp field variation. Unfortunately, this leads to an increase in the computational burden. An alternative solution is to increase the sampling density of the field components in the material interface region by use of a nonuniform PSTD algorithm with either a nonuniform FFT<sup>33</sup> or a uniform FFT combined with a coordinate transformation.<sup>34</sup> We found that another satisfactory solution is to introduce a less abrupt transition in the material properties at the interface. Here we simply average the dielectric constant of the core and cladding at the interface over one grid cell, as depicted by the solid

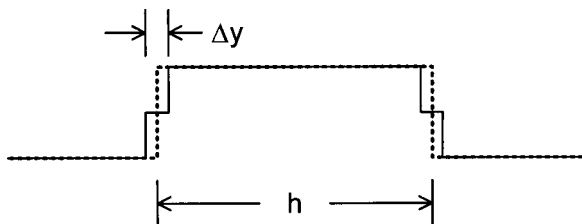


Fig. 6. Cross-sectional profile of the dielectric constant of the 2-D waveguide. The solid line represents the profile of the actual waveguide modeled in the test simulation.

line in Fig. 6. One could argue that the less abrupt transition in fact provides a more realistic representation of the transition of the material properties at a physical interface.

The dielectric constants of the core and cladding layers of the waveguide are assumed to be  $\epsilon_r = 4.84$  and  $\epsilon_r = 4.0$ , respectively. The thickness of the core, defined as  $h$  in Fig. 6, is 0.682  $\mu\text{m}$ . A ramped sinusoid is used to excite the fundamental wave, which is assumed to have a free-space wavelength of  $\lambda_0 = 1.5 \mu\text{m}$ . At this operating frequency, this waveguide supports only the fundamental mode. The fundamental mode is excited at the left end of the waveguide by a compact wave source condition.<sup>30</sup> The source consists of two adjacent linear arrays of hard sources, with each array spanning the cross section of the waveguide. The hard sources are weighted in the transverse direction by the estimated fundamental mode profile of the waveguide structure described by the solid line in Fig. 6. The 2-D computational domain is terminated by uniaxial PML absorbing boundary conditions.

### A. Linear Validations

Here we investigate the effect of the assumptions made in Eqs. (11) and (12) on the accuracy of PSTD-4 for the modeling of heterogeneous problems. Toward this end, we conduct simulations of fundamental mode propagation in a linear waveguide and compare the numerical and theoretical longitudinal propagation constants. For these tests, we use a grid-sampling density of roughly ten points per wavelength in the core region. Assuming the waveguide structure and operating frequency stated above, we calculate a theoretical propagation constant of  $\beta_T = 8.86575 \times 10^6$  rad/m for the fundamental mode.

First, we conduct the simulation using the PSTD-2 algorithm, which does not include higher-order terms requiring approximation in the manner of Eqs. (11) and (12). To focus our investigation on any difficulties caused by a material discontinuity, we choose an extremely small time step to minimize the numerical dispersion error. Here we choose a time step that is 16 times smaller than the 2-D stability limit given by<sup>27</sup>

$$\Delta t_s = \frac{2(\epsilon_r^{\text{clad}})^{1/2}}{\pi c(\Delta x^{-2} + \Delta y^{-2})^{1/2}}. \quad (28)$$

The propagation constant computed from the PSTD-2 simulation is  $\beta_{P2} = 8.86613 \times 10^6$  rad/m. Upon comparing  $\beta_{P2}$  with  $\beta_T$ , we can see that the PSTD-2 simulation with  $\Delta t = \Delta t_s/16$  yields an error of 0.00439%. This simulation result clearly shows that the material discontinuities of the waveguide do not cause any difficulties for this algorithm.

Second, we repeat the simulation using the PSTD-4 algorithm. Numerical errors in PSTD-4 include not only numerical dispersion, but also the effects of the assumptions made in Eqs. (11) and (12). Here a choice of a small time step would minimize both sources of error—an undesirable outcome given the goal of this investigation. Therefore we choose the maximum allowed time step  $\Delta t_s$  and compute a theoretical propagation constant that accounts for the effects of numerical dispersion. Specifically, we evaluate the numerical dielectric constant of the

core and cladding of the waveguide using the numerical dispersion relation of PSTD-4 presented in Eq. (21) for  $\Delta t = \Delta t_s$ . The dispersion-normalized theoretical propagation constant is  $\beta_{NT} = 8.86576 \times 10^6$  rad/m. (Note that because the numerical dispersion error of the PSTD-4 algorithm is so small, this dispersion-normalized constant is essentially identical to  $\beta_T$ .) Because the PSTD-2 simulation result has shown that the FFT-related errors associated with the material discontinuity are negligible, any deviation of the propagation constant in the PSTD-4 simulation represents the numerical error associated with the assumption made in Eqs. (11) and (12). The propagation constant computed from the PSTD-4 simulation is  $\beta_{P4} = 8.86654 \times 10^6$  rad/m. Upon comparing  $\beta_{P4}$  with  $\beta_{NT}$ , we can see that the PSTD-4 simulation yields an error of only 0.0088%. (A comparison between  $\beta_{P4}$  and  $\beta_T$  reveals that the total error for the PSTD-4 simulation, inclusive of numerical dispersion errors, is 0.0089%, assuming  $\Delta t = \Delta t_s$ .) This simulation result clearly shows that the effect of the assumptions made in Eqs. (11) and (12) is negligible. This investigation also further illustrates the enhanced accuracy of the PSTD-4 algorithm relative to PSTD-2.

## B. Nonlinear Validations

For the nonlinear simulations, we add an instantaneous second-order nonlinearity to the core of the waveguide. A QPM grating—a periodic reversal of the nonlinearity—is constructed in the nonlinear core. The grating is designed to restore the proper phase relationship between the fundamental wave and the second harmonic in the presence of dispersion, thereby improving the efficiency of second-harmonic generation. The sign (polarization) of  $\chi^{(2)}$  is constant over a length equal to the coherence length  $L_c$  defined as follows:

$$L_c = \frac{\pi}{|2\beta_f - \beta_s|} = \frac{\lambda_0^f}{4|n_{\text{eff}}^f - n_{\text{eff}}^s|}, \quad (29)$$

where  $\beta_f$  and  $\beta_s$  are the propagation constant of the fundamental and second harmonic, respectively;  $\lambda_0^f$  is the free-space wavelength of the fundamental wave; and  $n_{\text{eff}}^f$  and  $n_{\text{eff}}^s$  are the effective indices at the fundamental and second-harmonic frequencies, respectively.

The nonlinear core is modeled with  $\chi^{(2)} = 44$  pm/V, which corresponds to the nonlinear susceptibility of LiNbO<sub>3</sub>. The effective index for the fundamental mode is  $n_{\text{eff}} = 2.116$  at the operating wavelength of the fundamental wave ( $\lambda_0^f = 1.5$   $\mu\text{m}$ ). The free-space wavelength of the second harmonic is  $\lambda_0^s = 0.75$   $\mu\text{m}$ . At this wavelength, the waveguide supports a fundamental mode with  $n_{\text{eff}} = 2.163$  as well as a higher-order mode with  $n_{\text{eff}} = 2.063$ . The simulated peak power density of the mode profile of this incident wave is  $2.245 \times 10^{12}$  W/m<sup>2</sup>. The QPM grating, which is designed for the fundamental waveguide mode, assumes that  $L_c = 7.885$   $\mu\text{m}$ .

PSTD-2, PSTD-4, and FDTD simulations of the waveguide are conducted. In each simulation, a discrete Fourier transform at the second-harmonic frequency is applied to the fields along the center axis of the waveguide and the power density is computed.

First, we compare the accuracy and computational efficiency of PSTD-2 and PSTD-4 simulations for modeling second-harmonic generation in a 130- $\mu\text{m}$ -long version of the waveguide described above. We assume a grid-sampling density of roughly ten points per wavelength for the fundamental wave in the core region. The specific grid cell dimensions ( $\Delta x = 67.4$  nm and  $\Delta y = 62.0$  nm) are chosen so that an integer number of grid cells fit within each homogeneous section of the waveguide; that is,  $L_c = 117\Delta x$  and  $h = 11\Delta y$ . The maximum allowed time step is given by the 2-D stability limit<sup>27</sup>:

$$\Delta t_s = \frac{2(\epsilon_r^{\text{clad}})^{1/2}}{\pi c(\Delta x^{-2} + \Delta y^{-2})^{1/2}}, \quad (30)$$

where  $\epsilon_r^{\text{clad}}$  is the dielectric constant of the cladding region. We note that this is the stability limit for the linear case. In contrast to the previous 1-D example, the stability limit in two dimensions was not affected by the introduction of the nonlinearity.

Starting with  $\Delta t_s$ , the PSTD-2 and PSTD-4 simulations are repeated with smaller time steps until numerical convergence in the power density is reached. The convergence test results for PSTD-2 are shown in Fig. 7(a). We can see that the power density of the second harmonic is grossly underestimated when PSTD-2 is used

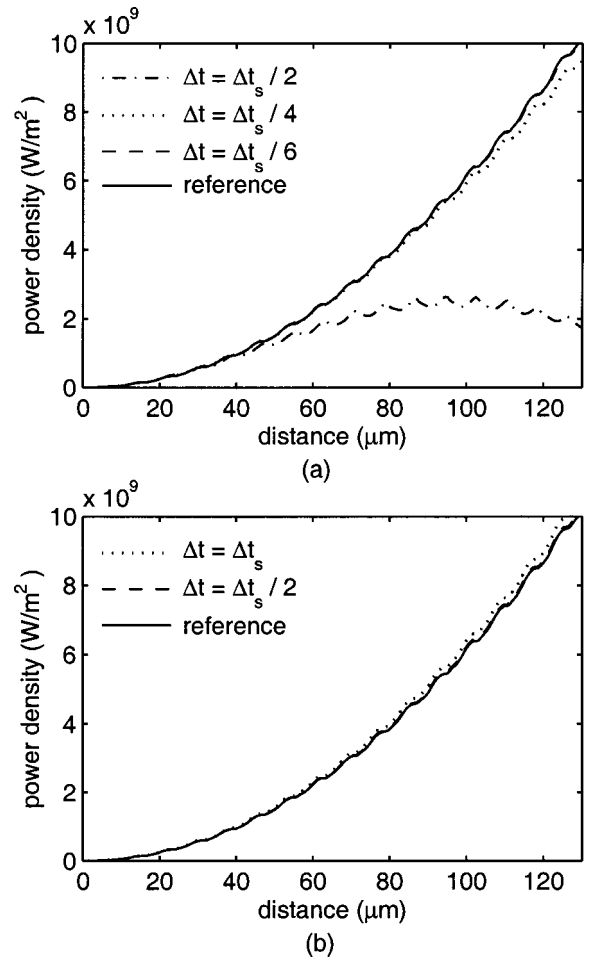


Fig. 7. Convergence tests for (a) PSTD-2 and (b) PSTD-4. The power density of the second-harmonic wave is computed from PSTD simulations with different time steps.

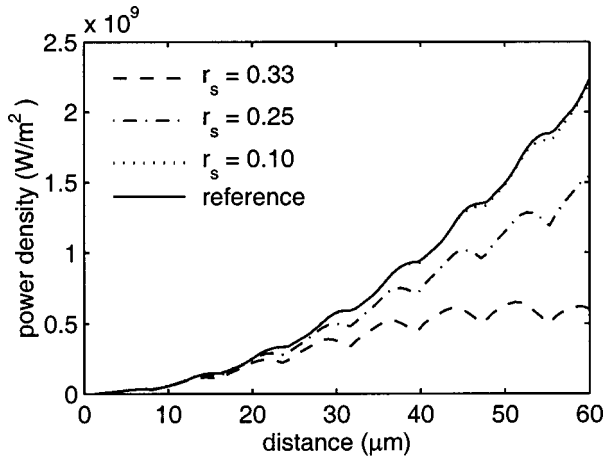


Fig. 8. Convergence test for FDTD. The power density of the second-harmonic wave is computed from FDTD simulations with different grid resolutions. The FDTD grid cell size is expressed as a fraction of the PSTD-4 grid cell size.

with a large time step, but does converge to the reference data ( $\Delta t = \Delta t_s/30$ ) as the time step is decreased. The convergence test results for PSTD-4 are shown in Fig. 7(b). PSTD-4 slightly overestimates the power density of the second harmonic when the maximum possible time step is used and quickly converges to the reference data ( $\Delta t = \Delta t_s/6$ ) with a small decrease in the time step.

For a quantitative comparison of the computational efficiencies, we estimate the time step required in each method to achieve an error of no more than  $\sim 2\%$  in the computed power density at a propagation distance of  $130 \mu\text{m}$ . The required time steps are  $\Delta t = \Delta t_s/5$  (error of approximately  $-2.5\%$ ) and  $\Delta t = \Delta t_s/1.5$  (error of approximately  $+1.5\%$ ) for PSTD-2 and PSTD-4, respectively. We measured the actual CPU time on a Sun Ultra 80 workstation by multiplying the CPU run time per time step by the total number of time steps required to complete the simulation. The CPU requirements per time step are  $0.523$  and  $1.17$  s for the PSTD-2 and PSTD-4 simulations, respectively. Approximately  $21,870$  PSTD-2 time steps and  $6560$  PSTD-4 time steps are required to propagate the wave a distance of  $130 \mu\text{m}$ . Hence the total CPU time for PSTD-2 is  $11,450$  s whereas PSTD-4 takes  $7680$  s. Thus PSTD-4 is approximately  $1.5$  times faster than PSTD-2 in this specific example. As mentioned in the above 1-D example, the efficiency of PSTD-4 relative to PSTD-2 is proportional to the overall size of the model.

Finally, we compare the accuracy and computational efficiency of PSTD-4 and FDTD. Because the numerical dispersion error in FDTD is directly controlled by the spatial grid resolution, we gradually reduce the grid cell size until FDTD achieves comparable accuracy to the PSTD-4 method. The simulation results are presented in Fig. 8 for a  $60\text{-}\mu\text{m}$  propagation distance. A smaller computational domain is used in this test case because of the increased computational burden associated with FDTD. In Fig. 8, the grid resolution used in the FDTD simulations is stated in terms of the following ratio:  $r_s \equiv \Delta x_{\text{FDTD}}/\Delta x_{\text{PSTD}} = \Delta y_{\text{FDTD}}/\Delta y_{\text{PSTD}}$ . We find that the FDTD error drops to approximately  $2\%$  when the grid cell size is decreased by a factor of ten relative to PSTD-4. With  $r_s = 0.1$ , the CPU times per time step are  $5.94$  and

$0.536$  s for the FDTD and PSTD-4 simulations, respectively. Approximately  $14,000$  FDTD time steps ( $\Delta t = \Delta t_s$ ) and  $2990$  PSTD-4 time steps ( $\Delta t = \Delta t_s/1.5$ ) are required to propagate the wave a distance of  $60 \mu\text{m}$ . Therefore the total CPU times for the entire simulation are  $83,200$  and  $1620$  s for FDTD and PSTD-4, respectively. These numbers indicate that PSTD-4 is approximately  $51$  times faster than FDTD in this example.

## 6. NUMERICAL APPLICATION: SECOND-HARMONIC GENERATION IN A TILTED QUASI-PHASE-MATCHING GRATING

To illustrate a practical application of the PSTD algorithms developed in the above sections, we consider a 2-D QPM grating structure oriented at an oblique angle with respect to the direction of propagation of the incident fundamental wave.<sup>35</sup> Figure 9 shows the phase-matching configuration for second-harmonic generation in this structure. The wave vectors of the fundamental wave and the second-harmonic wave are denoted as  $\mathbf{k}_f$  and  $\mathbf{k}_s$ , respectively. In the conventional case of an input fundamental wave at normal incidence with respect to the grating (i.e.,  $\phi = 90^\circ$  in Fig. 9), the fundamental and second-harmonic waves are collinear (i.e.,  $\theta = 0^\circ$ ). However, in the case considered here, where  $\phi < 90^\circ$ , the second-harmonic wave emerges with a different angle of propagation. The magnitude of  $\mathbf{k}_g$ , the reciprocal lattice vector associated with the grating, is determined by  $k_g = 2\pi/d$ , where  $d$  is the spatial period of the grating. With this configuration, the 2-D phase-matching condition is given by

$$2\mathbf{k}_f + \mathbf{k}_g = \mathbf{k}_s. \quad (31)$$

We note that the algorithms presented in the above sections do not include the physics of material dispersion. It is straightforward, but beyond the scope of this paper, to extend these algorithms with an auxiliary differential equation technique<sup>36</sup> to permit the modeling of dispersive materials. Here we limit our investigation to the case of

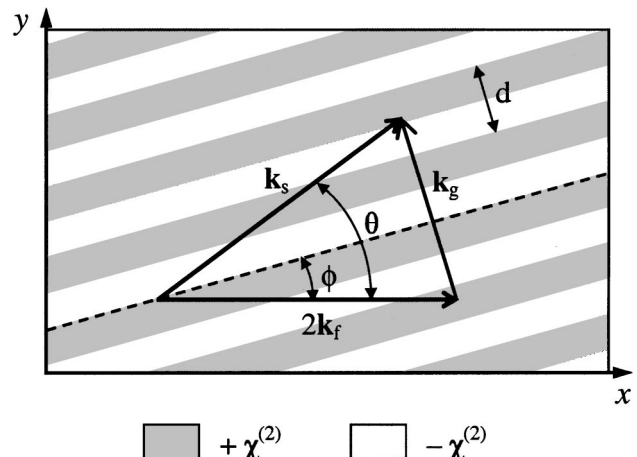


Fig. 9. Schematic diagram of the phase-matching condition for second-harmonic generation in a QPM grating structure oriented at an oblique angle with respect to the direction of propagation of the incident fundamental wave.

a medium with frequency-independent optical properties, which allows for the direct implementation of the algorithms as presented. In the absence of material dispersion,  $2k_f = k_s$ . From the phase-matching diagram in Fig. 9, it follows that

$$\theta = 2\phi, \quad (32)$$

$$d = \frac{\lambda_0^f}{4n \sin \phi}. \quad (33)$$

Here  $n$  represents the index of refraction of the medium.

We use the PSTD-4 algorithm to model the tilted QPM grating. A 2-D computational domain is constructed by use of a uniform lattice. The  $x$  axis of the grid is aligned with the direction of propagation of the fundamental wave. In other words, the QPM grating is oriented an angle  $\phi$  with respect to the  $x$  axis, as shown in Fig. 9. The material parameters are chosen to be  $n = 2.2$  and  $\chi^{(2)} = 44 \times 10^{-12}$  m/V, which are similar to those of LiNbO<sub>3</sub>. The wavelength of the fundamental wave is 1.5  $\mu$ m. The grid resolution for  $\Delta x$  and  $\Delta y$  is chosen to yield approximately five points per wavelength of the second harmonic.

We excited the fundamental wave near the left boundary of the domain using a compact wave source condition that is compatible with the PSTD algorithm and designed to generate a plane wave propagating in the  $x$  direction. That is, we introduce two adjacent linear arrays of equally weighted hard sources spanning the entire extent of the grid in the  $y$  direction. The power density of the fundamental wave is  $7.766 \times 10^{11}$  W/m<sup>2</sup>.

We can reduce the overall size of a computational domain using periodic boundary conditions to terminate the top and bottom boundaries. The left and right grid boundaries are terminated with a uniaxial PML. The longitudinal dimension of the computational domain is chosen to be  $x_{\max} = 137.2 \mu$ m with 125  $\mu$ m between the source plane and the right uniaxial PML boundary. The transverse dimension is chosen to be  $y_{\max} = my_p$ , where  $m$  is an integer and  $y_p = d/\cos \phi$  is the projection of the grating period along the  $y$  axis. To confirm the validity of the periodic boundary conditions, we compared the field values in a smaller computational domain (smaller  $m$ ) with the corresponding field values in a larger computational domain (larger  $m$ ) and found essentially no difference.

We investigate three different QPM gratings designed for  $\phi = 5^\circ$ ,  $10^\circ$ , and  $15^\circ$ , which correspond to second-harmonic angles of propagation of  $\theta = 10^\circ$ ,  $20^\circ$ , and  $30^\circ$ , respectively. For each of these cases, the PSTD-4 simulation is run until the sinusoidal steady state has been reached at every point in the grid. Then we apply a discrete Fourier transform to the electric and magnetic fields over the entire domain, selecting the frequency to be that of the second harmonic. Finally, we use this phasor field data to compute the time-averaged Poynting vector over the entire domain to track both the intensity and the direction of power flow of the second harmonic.

To investigate second-harmonic generation as a function of the distance propagated by the fundamental wave, we take an average of all the Poynting vectors calculated along the  $y$  direction at a given position along the  $x$  axis.

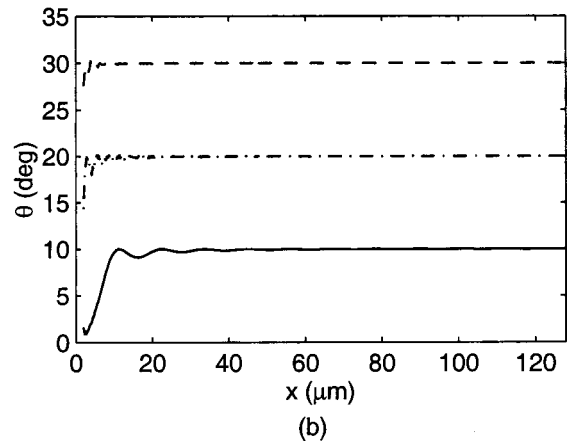
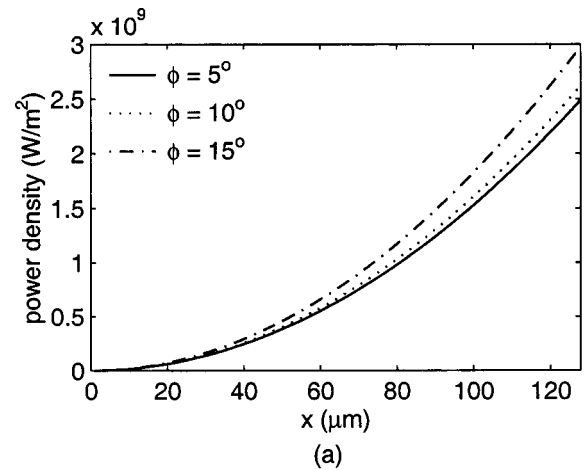


Fig. 10. (a) Power density and (b) direction of power flow of the second harmonic generated in three different QPM gratings, as a function of distance propagated by the fundamental wave.

We repeat this calculation for a number of positions along the  $x$  axis. Figure 10 shows the power density and the average propagation angle for the second-harmonic wave as a function of  $x$ . As expected, the results in Fig. 10(a) indicate that gratings designed for larger  $\phi$  produce higher frequency conversion efficiency for the same propagation distance of the fundamental wave. In Fig. 10(b), we can see that a finite distance of propagation is required for the second-harmonic wave to settle into a well-defined propagation angle. We also note that the terminal propagation angle is in excellent agreement with the design angle. For example, the simulation results for the  $\phi = 5^\circ$  case indicate that a propagation distance of approximately 40  $\mu$ m is for the propagation angle to converge to the design angle of  $\theta = 10^\circ$ . This distance decreases as the grating angle increases.

## 7. CONCLUSIONS

We have developed and validated two PSTD schemes for solving the time-domain nonlinear Maxwell's equations. First, an existing PSTD-2 formulation was adapted to model the optical wave propagation in  $\chi^{(2)}$  materials. Second, a PSTD-4 scheme was formulated to further enhance the numerical accuracy. These low-dispersion schemes permit use of coarser grid resolutions than

FDTD. Consequently, both PSTD methods offer significant advantages over the standard FDTD scheme in terms of computational accuracy and efficiency, as demonstrated with the series of benchmark simulations presented here. Because errors due to numerical dispersion are cumulative, the computational savings of PSTD-4 over PSTD-2 and FDTD increases with distance of wave propagation. Hence PSTD-4 (as well as PSTD-2) makes it possible to more efficiently model frequency conversion processes in larger-scale nonlinear optical structures. Finally, to illustrate an application of the algorithms developed here, we provided a brief numerical study of second-harmonic generation in tilted QPM gratings using PSTD-4. Once again, we note that the formulations presented here can be directly extended to include material dispersion by an auxiliary differential equation technique similar to that developed for FDTD.

## ACKNOWLEDGMENTS

This research was supported by the National Science Foundation Presidential Early Career Award for Scientists and Engineers ECS-9985004. Computing resources were provided in part by Cray, Inc.

## REFERENCES

- M. H. Chou, I. Brener, M. M. Fejer, E. E. Chaban, and S. B. Christman, "1.5- $\mu\text{m}$ -band wavelength conversion based on cascaded second-order nonlinearity in  $\text{LiNbO}_3$  waveguides," *IEEE Photon. Technol. Lett.* **11**, 653–655 (1999).
- Y. Baek, R. Schiek, G. I. Stegeman, G. Krijnen, I. Baumann, and W. Sohler, "All-optical integrated Mach-Zehnder switching due to cascaded nonlinearities," *Appl. Phys. Lett.* **68**, 2055–2057 (1996).
- G. Y. Wang, J. Zhao, Q. Chen, and M. Cronin-Golomb, "Widely tunable efficient intracavity quasiphase-matched midinfrared generation," *Appl. Phys. Lett.* **70**, 2218–2220 (1997).
- G. W. Ross, M. Pollnau, P. G. R. Smith, W. A. Clarkson, P. E. Britton, and D. C. Hanna, "Generation of high-power blue light in periodically poled  $\text{LiNbO}_3$ ," *Opt. Lett.* **23**, 171–173 (1998).
- J. A. Armstrong, N. Bloembergen, J. Ducuing, and P. S. Pershan, "Interactions between light waves in a nonlinear dielectric," *Phys. Rev.* **127**, 1918 (1962).
- B. Hermansson, D. Yevick, and L. Thylen, "A propagating beam method analysis of nonlinear effects in optical waveguides," *Opt. Quantum Electron.* **16**, 525–534 (1984).
- K. Hayata and M. Koshiba, "Numerical study of guided-wave sum-frequency generation through second-order nonlinear parametric processes," *J. Opt. Soc. Am. B* **8**, 449–458 (1991).
- P. S. Weitzman and U. Osterberg, "A modified beam propagation method to model second harmonic generation in optical fibers," *IEEE J. Quantum Electron.* **29**, 1437–1443 (1993).
- H. M. Masoudi and J. M. Arnold, "Modeling second-order nonlinear effects in optical waveguides using a parallel-processing beam propagation method," *IEEE J. Quantum Electron.* **31**, 2107–2113 (1995).
- H. F. Chou, C. F. Lin, and S. Mou, "Comparisons of finite difference beam propagation methods for modeling second-order nonlinear effects," *J. Lightwave Technol.* **17**, 1481–1486 (1999).
- A. Taflove and S. C. Hagness, *Computational Electrodynamics: The Finite-Difference Time-Domain Method* (Artech House, Norwood, Mass., 2000).
- A. Mekis, J. C. Chen, I. Kurland, S. H. Fan, P. R. Villeneuve, and J. D. Joannopoulos, "High transmission through sharp bends in photonic crystal waveguides," *Phys. Rev. Lett.* **77**, 3787–3790 (1996).
- B. D'Urso, O. Painter, J. O'Brien, T. Tombrello, A. Yariv, and A. Scherer, "Modal reflectivity in finite-depth two-dimensional photonic-crystal microcavities," *J. Opt. Soc. Am. B* **15**, 1155–1159 (1998).
- M. Boroditsky, T. F. Krauss, R. Coccioli, R. Vrijen, R. Bhat, and E. Yablonovitch, "Light extraction from optically pumped light-emitting diode by thin-slab photonic crystals," *Appl. Phys. Lett.* **75**, 1036–1038 (1999).
- R. W. Ziolkowski and M. Tanaka, "FDTD analysis of PBG waveguides, power splitters and switches," *Opt. Quantum Electron.* **31**, 843–855 (1999).
- S. C. Hagness, D. Rafizadeh, S. T. Ho, and A. Taflove, "FDTD microcavity simulations: design and experimental realization of waveguide-coupled single-mode ring and whispering-gallery-mode disk resonators," *J. Lightwave Technol.* **15**, 2154–2165 (1997).
- B. E. Little, J. S. Foresi, G. Steinmeyer, E. R. Thoen, S. T. Chu, H. A. Haus, E. P. Ippen, L. C. Kimerling, and W. Greene, "Ultra-compact Si-SiO<sub>2</sub> microring resonator optical channel dropping filters," *IEEE Photon. Technol. Lett.* **10**, 549–551 (1998).
- R. X. Bian, R. C. Dunn, and X. S. Xie, "Single molecule emission characteristics in near-field microscopy," *Phys. Lett. A* **75**, 4772–4775 (1995).
- G. Liu, J. F. Seurin, S. L. Chuang, D. I. Babic, S. W. Corzine, M. Tan, D. C. Barness, and T. N. Tiouririne, "Mode selectivity study of vertical-cavity surface-emitting lasers," *Appl. Phys. Lett.* **73**, 726–728 (1998).
- T. W. Lee, S. C. Hagness, D. L. Zhou, and L. J. Mawst, "Modal characteristics of ARROW-type vertical-cavity surface-emitting lasers," *IEEE Photon. Technol. Lett.* **13**, 770–772 (2001).
- D. W. Prather and S. Y. Shi, "Formulation and application of the finite-difference time-domain method for the analysis of axially symmetric diffractive optical elements," *J. Opt. Soc. Am. A* **16**, 1131–1142 (1999).
- P. M. Goorjian, A. Taflove, R. M. Joseph, and S. C. Hagness, "Computational modeling of femtosecond optical solitons from Maxwell's equations," *IEEE J. Quantum Electron.* **28**, 2416–2422 (1992).
- R. W. Ziolkowski and J. B. Judkins, "Full-wave vector Maxwell equation modeling of the self-focusing of ultrashort optical pulses in a nonlinear Kerr medium exhibiting a finite response time," *J. Opt. Soc. Am. B* **10**, 186–198 (1993).
- D. M. Sullivan, "Nonlinear FDTD formulation using Z transforms," *IEEE Trans. Microwave Theory Tech.* **43**, 676–682 (1995).
- A. Bourgeade and E. Freysz, "Computational modeling of second-harmonic generation by solution of full-wave vector Maxwell equations," *J. Opt. Soc. Am. B* **17**, 226–234 (2000).
- R. M. Joseph and A. Taflove, "FDTD Maxwell's equations models for nonlinear electrodynamics and optics," *IEEE Trans. Antennas Propag.* **45**, 364–374 (1997).
- Q. H. Liu, "The PSTD algorithm: a time-domain method requiring only two cells per wavelength," *Microwave Opt. Technol. Lett.* **15**, 158–165 (1997).
- B. Fornberg, *A Practical Guide to Pseudospectral Methods* (Cambridge U. Press, Cambridge, UK, 1996).
- Q. H. Liu, "Large-scale simulations of electromagnetic and acoustic measurements using the pseudo-spectral time-domain (PSTD) algorithm," *IEEE Trans. Geosci. Remote Sens.* **37**, 917–926 (1999).
- T. W. Lee and S. C. Hagness, "A compact wave source condition for the pseudospectral time-domain method," *IEEE Wireless Propag. Lett.* (to be published).
- J. Fang, "Time-domain finite-difference computations for Maxwell's equations," Ph.D. dissertation (Department of Electrical Engineering and Computer Sciences, University of California, Berkeley, Berkeley, Calif., 1989).

32. R. W. Ziolkowski, "The incorporation of microscopic material models into the FDTD approach for ultrashort optical-pulse simulation," *IEEE Trans. Antennas Propag.* **45**, 375–391 (1997).
33. Q. H. Liu and N. Nguyen, "An accurate algorithm for non-uniform fast Fourier transform (NUFFT)," *IEEE Microwave Guid. Wave Lett.* **8**, 18–20 (1998).
34. W. K. Leung, Y. Chen, and R. Mittra, "Transformed-space non-uniform pseudo-spectral time-domain (NU-PSTD) algorithm without use of non-uniform FFT," in *IEEE AP-S International Symposium* (Institute of Electrical and Electronics Engineers, Piscataway, N.J., 2001), pp. 498–501.
35. S. T. Yang and S. P. Velsko, "Frequency-agile kilohertz repetition-rate optical parametric oscillator based on periodically poled lithium niobate," *Opt. Lett.* **24**, 133–135 (1999).
36. R. M. Joseph, S. C. Hagness, and A. Taflove, "Direct time integration of Maxwell's equations in linear dispersive media with absorption for scattering and propagation of femtosecond electromagnetic pulses," *Opt. Lett.* **16**, 1412–1414 (1991).